Investigation on p-type doping of PBn unipolar barrier InAsSb photodetectors

ZHANG Jian[1], CHANG Chao[1], LI Hong-Fu[1], SHI Yu-Na[1], YIN Han-Xiang[1], LI Yan-Hui[1], YUE Biao[1], WANG Hai-Peng[1,2], YAN Chang-Shan[1], DAI Xin-Ran[1], DENG Gong-Rong[1*], KONG Jin-Cheng[1], ZHAO Peng[1*], ZHAO Jun[1*]

（1. Kunming Institute of Physics, Kunming 650223, China;
2. Beijing Engineering Research Center of Mixed Reality and Advanced Display, School of Optics and Photonics, Beijing Institute of Technology, Beijing 100081, China）

Abstract：The lattice-matched XBn structures of InAsSb, grown on GaSb substrates, exhibit high crystal quality, and can achieve extremely low dark currents at high operating temperatures (HOT). Its superior performance is attributed to the unipolar barrier, which blocks the majority carriers while allowing unhindered hole transport. To further explore the energy band and carrier transport mechanisms of the XBn unipolar barrier structure, this paper systematically investigates the influence of doping on the dark current, photocurrent, and tunneling characteristics of InAsSb photodetectors in the PBn structure. Three high-quality InAsSb samples with unintentionally doped absorption layers (AL) were prepared, with varying p-type doping concentrations in the GaSb contact layer (CL) and the AlAsSb barrier layer (BL). As the p-type doping concentration in the CL increased, the device's turn-on bias voltage also increased, and p-type doping in the BL led to tunneling occurring at lower bias voltages. For the sample with UID BL, which exhibited an extremely low dark current of 5×10^{-6} A/cm^2. The photocurrent characteristics were well-fitted using the back-to-back diode model, revealing the presence of two opposing space charge regions on either side of the BL.

Key words：InAsSb, PBn, p-type doping, dark current

PBn 单极势垒型 InAsSb 光电探测器 p 型掺杂研究

张 健[1]，常 超[1]，李红福[1]，石玉娜[1]，殷瀚翔[1]，李艳辉[1]，岳 彪[1]，王海澎[1,2]，闫常善[1]，戴欣冉[1]，邓功荣[1*]，孔金丞[1]，赵 鹏[1*]，赵 俊[1*]

（1. 昆明物理研究所，云南 昆明 650223；
2. 北京理工大学 光学与光子学院 北京市混合现实与先进显示工程技术研究中心，北京 100081）

摘要：在 GaSb 衬底上外延生长晶格匹配的 XBn 结构 InAsSb 具有高晶体质量，在高工作温度(HOT)下能够实现极低的暗电流。该结构具有优越的性能，在阻挡多数载流子的同时，不影响空穴传输。为了进一步探索 XBn 单极势垒结构的能带和载流子输运机理，系统地研究了掺杂对 PBn 结构 InAsSb 光电探测器的暗电流、光电流和隧穿特性的影响。制备了三个高质量 InAsSb 样品，吸收层(AL)均为非故意掺杂(UID)，对接触层(CL)和势垒层(BL)进行不同浓度的 p 型掺杂。随着 CL 中 p 型掺杂浓度的增加，器件的开启偏压变大，而 BL 中的 p 型掺杂会导致隧穿效应发生在更低的偏置电压下。对于 BL 非故意掺杂的样品，表现出极低的暗电流，仅为 5×10^{-6} A/cm^2。该样品的器件光电流特性可以通过背靠背二极管模型拟合，揭示了 BL 两侧存在两个反向的空间电荷区。

关 键 词：铟砷锑；PBn；p 型掺杂；暗电流

中图分类号：O475　　**文献标识码**：A

Introduction

With exceptional atmospheric transparency，the mid-wave infrared（MWIR）region plays a vital role in various critical imaging applications. In comparison to the short-wave infrared（SWIR），MWIR offers a stronger signal and improved night vision performance. Furthermore，MWIR boasts superior refractive limit resolution compared to long-wave infrared（LWIR）and benefits from better sensitivity due to the more substantial variation of the blackbody radiation curve with temperature.

Recent advances in InAsSb-based MWIR photodetectors have demonstrated high performance at elevated operating temperatures，outperforming conventional InSb detectors that require operation at temperatures in the liquid nitrogen range[1-7]. The primary source of dark current in InSb detectors is the generation of carriers in the depletion region due to Shockley Read-Hall（SRH）Generation-Recombination（G-R）centers[8-9].

To address these limitations，high-quality InAsSb-based XBn structure infrared detectors can be grown on GaSb substrates. These detectors incorporate a wide energy gap barrier with a low valence band offset，effectively blocking the electronic component of current in the n-type absorber while allowing unimpeded minority hole transport through the barrier layer[6]. Consequently，the reduced depletion region in the narrow gap absorber of the barrier heterostructure suppresses the thermal generation of carriers，a significant source of dark current in the narrow gap absorber. In contrast，the thermal effects on the wide bandgap barrier are negligible，when in the depleted state.

While there is a wealth of theoretical literature on the doping of barrier layers in XBn structures[10-13]，few experimental studies have been reported[14, 15]. In our study，we focus on high-quality PBn unipolar barrier InAsSb materials grown on GaSb substrates. We investigate the light response and dark current characteristics of PBn InAsSb for varying p-type doping concentrations in both the contact layer（CL）and barrier layer（BL）. Additionally，we perform a detailed analysis of the valence band and tunneling characteristics.

1　Experiment

We grew high-quality lattice-matched InAsSb materials using molecular beam epitaxy on GaSb substrates. The growth process involved several key steps：initially，the GaSb substrate underwent degassing at 350 °C for 30 minutes in a pre-degassing chamber to eliminate adsorbed surface gases. Subsequently，the GaSb substrate was transferred to the growth chamber，where deoxidation occurred at 520 °C under a Sb atmosphere. Following deoxidation，a 250 nm GaSb buffer layer was grown at 500 °C to smoothen the surface. Subsequently，a 3 μm InAs$_{0.905}$Sb$_{0.095}$ absorption layer（AL）was grown at 440 °C，followed by a 150 nm AlAs$_{0.92}$Sb$_{0.08}$ barrier layer.

It′s important to note that GaSb exhibits a thermal expansion coefficient（TEC）of approximately 7. 75×10^{-6}°C^{-1}，which is about 1. 5 times greater than InAs（4. 52×10^{-6}°C^{-1}）

and InSb（5. 37 × 10^{-6} °C^{-1}）[16]. This TEC difference results in a Sb composition of around 9% on GaSb at room temperature for lattice-matched InAsSb. To mitigate strain during the growth process and attain high crystal quality，the Sb composition of the AL was set at 9. 5%. Finally，a 300 nm Be-doped p-type GaSb electrode layer was grown. Figure 1 illustrates the layer structure of the InAsSb films.

To prevent the space charge region from extending too deeply into the AL，which could increase the G-R current，we maintained the AL and the first half of the BL as unintentionally doped. Adjustments to the p-type doping concentration were made in the second half of the BL and the CL，and this approach led to the fabrication of InAsSb unit photodetectors. Table 1 provides an overview of the p-type doping concentrations for the three PBn structure samples.

The properties of InAsSb material were assessed using Fourier-transform infrared（FTIR）spectroscopy and Nomarski microscopy. Photodetector processing involved inductively coupled plasma（ICP）dry etching，SiO$_2$ surface passivation，and Ti/Au electrode deposition. The photo-response and temperature-variable dark current characteristics of the photodetectors were examined using a probe system，B1500A semiconductor parameter test system，and a temperature-variable metal Dewar. To calculate the energy band structure of PBn InAsSb photodetectors，we utilized Silvaco software.

Table 1　The p-type doping concentration of InAsSb samples
表 1　InAsSb 样品的 p 型掺杂浓度

Sample Number	CL	BL	AL
Sample A	5×10^{17} cm^{-3}	75nm（1×10^{14} cm^{-3} graded to 3×10^{17} cm^{-3}）+ 75nm UID	UID
Sample B	1. 5×10^{17} cm^{-3}	75nm（1×10^{14} cm^{-3} graded to 3×10^{17} cm^{-3}）+ 75nm UID	UID
Sample C	1. 5×10^{17} cm^{-3}	UID	UID

The Sb composition in both InAsSb and AlAsSb was precisely tuned to 9. 5% and 8%，respectively. At 300 K，the cutoff wavelength of InAsSb was determined to be 4. 5 μm，as measured through FTIR transmission spectroscopy（as shown in Fig. 1（b）). The surface morphology of InAsSb material was examined using a Nomarski microscope，revealing a remarkably low defect density of less than 300 cm^{-2}. The HRXRD analysis yielded a FWHM of 27 arcsecs for InAsSb. The combination of a high uniform HRTEM，a low FWHM，and a smooth surface（see Fig. 2）indicates the high quality of the material.

2　Results

We fabricated unit cell photodetectors with a size of 200 μm×200 μm，and we conducted measurements of photocurrent and dark current（J_{dark}）in the temperature range from 77 K to 300 K. Furthermore，we investigated the Activation Energy（E_a）using Arrhenius equation un-
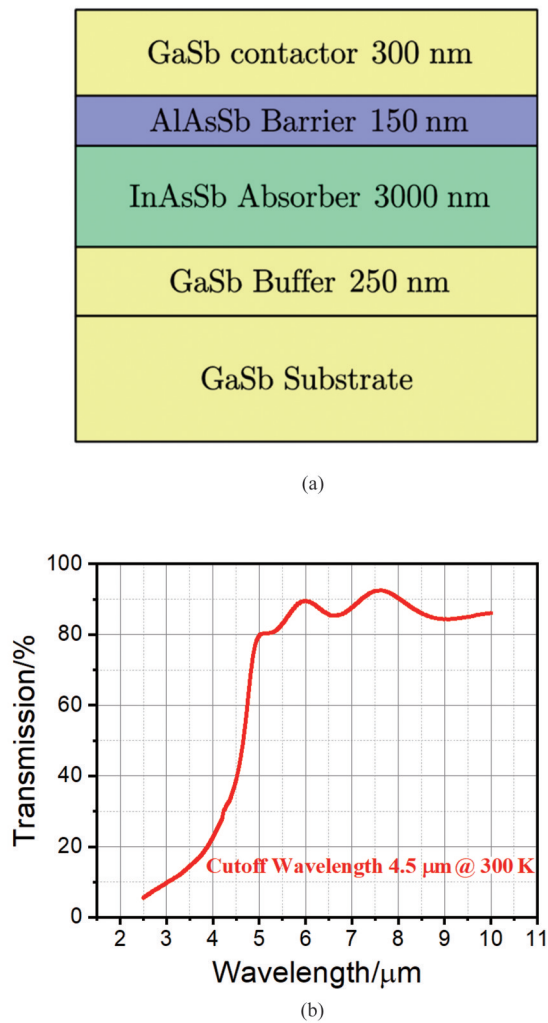
(a)

(b)

Fig. 1 (a) The PBn structure, GaSb(P)/AlAsSb(B)/InAsSb(n); (b) the FTIR spectrum reveals that the cutoff wavelength of the InAsSb film is 4.5 μm at 300 K

图 1 (a) PBn InAsSb 结构示意图, 包含 GaSb(P)/AlAsSb(B)/In-AsSb(n);(b)FTIR 光谱显示, 在 300 K 下, InAsSb 薄膜的截止波长为 4.5 μm

der varying temperature conditions[17].

In Fig. 3(a), the dark current of sample A is presented, measured in the temperature range from 77 K to 287 K. In this sample, the CL is p-type doped at a concentration of 5×10^{17} cm^{-3}, and the BL is composed of a 75 nm layer (p-type doped ranging from 1×10^{14} cm^{-3} to 3×10^{17} cm^{-3}) followed by a 75 nm UID layer. Notably, the turn-on voltage for this sample is approximately -0.2 V, and a 'second plateau' with a turn-on voltage of around -0.5 V is observed. This effect is attributed to the higher p-type doping in the CL (5×10^{17} cm^{-3}), which surpasses the BL doping and introduces a hole trap between the CL and the BL.

Figure 3(b) shows the dark current of sample B, which was measured within the temperature range from 77 K to 277 K. In this case, the CL is p-type doped at a concentration of 1.5×10^{17} cm^{-3}, lower than the CL in sample A (5×10^{17} cm^{-3}) and matching the BL's doping level

(3×10^{17} cm^{-3}). By reducing the p-type doping in the CL, the 'second plateau' turn-on voltage disappears.

Figure 3(c) displays the dark current characteristics of sample C, measured over the same temperature range. In this sample, the CL is p-type doped at 1.5×10^{17} cm^{-3}, while the BL remains unintentionally doped. Notably, the dark current of sample C is one order of magnitude lower than samples A and B at positive bias, and the turn-on voltage of -2 V significantly surpasses the values for samples A and B (-1.4 V and -0.4 V, respectively). At -0.5 V and 150 K, the dark current for sample C is approximately 5×10^{-6} A/cm^2.

Analyzing the photodetector's dark current *I-V* test results, the conclusions are as follows:

1) Higher p-type doping in the BL results in easier tuning under high reverse bias, as demonstrated by the dark current characteristics of samples B and C.

2) Sample A exhibits a higher p-type doping concentration in the CL compared to the BL, introducing a hole trap that forms a valence band barrier, consequently raising the turn-on and tuning voltage.

3) In the case of sample C, the UID BL effectively blocks majority carriers, both electrons from the AL and holes from the CL. This suggests that the UID BL serves as a complementary barrier.

The Arrhenius fitting results of dark current in Fig. 4 (a)-(c) indicate that E_a falls within the temperatures spanning from 250 K to 150 K and the applied reverse bias increases from 0 V to 3 V. The activation energy for both diffusion current and G-R current can be reasonably approximated as:

$$J_{\text{diff}} = A_{\text{th}} \times e^{-\frac{E_G}{k_B T}} \quad , \quad (1)$$

$$J_{\text{G-R}} = A_{\text{th}} \times e^{-\frac{E_G}{2k_B T}} \quad . \quad (2)$$

When the calculated E_a matches the energy band gap (E_G), the dark current is dominated by the diffusion current. Conversely, when E_a corresponds to half of the energy band gap ($E_G/2$), the dark current is predominantly governed by the G-R current. At a temperature of 150 K, the activation energy is measured approximately 200 meV, and the proportion of G-R current within the dark current becomes more prominent.

At reverse bias voltages lower than 2.0 V, the E_a values for all three samples surpass 250 meV at 250 K. However, as the applied reverse bias voltage exceeds 2.0 V, the E_a values exhibit varying trends. Samples A and C experience a slight decrease in E_a, while sample B's E_a significantly drops to 100 mV. Because the p-type doping of the CL at 1.5×10^{17} cm^{-3} is lower than the doping level of the BL at 3×10^{17} cm^{-3} in sample B, this lower p-type doping facilitates easier tuning at the interface between the CL and the BL under high reverse bias.

In contrast, in sample A, where the p-type doping of CL (5×10^{17} cm^{-3}) exceeds that of BL (3×10^{17} cm^{-3}), the majority electron current and minority hole carriers may be blocked, resulting in a drop in E_a as bias decreases under low reverse bias voltage at 150 K.

Through an analysis of the dark current and E_a characteristics, it becomes apparent that there may exist two
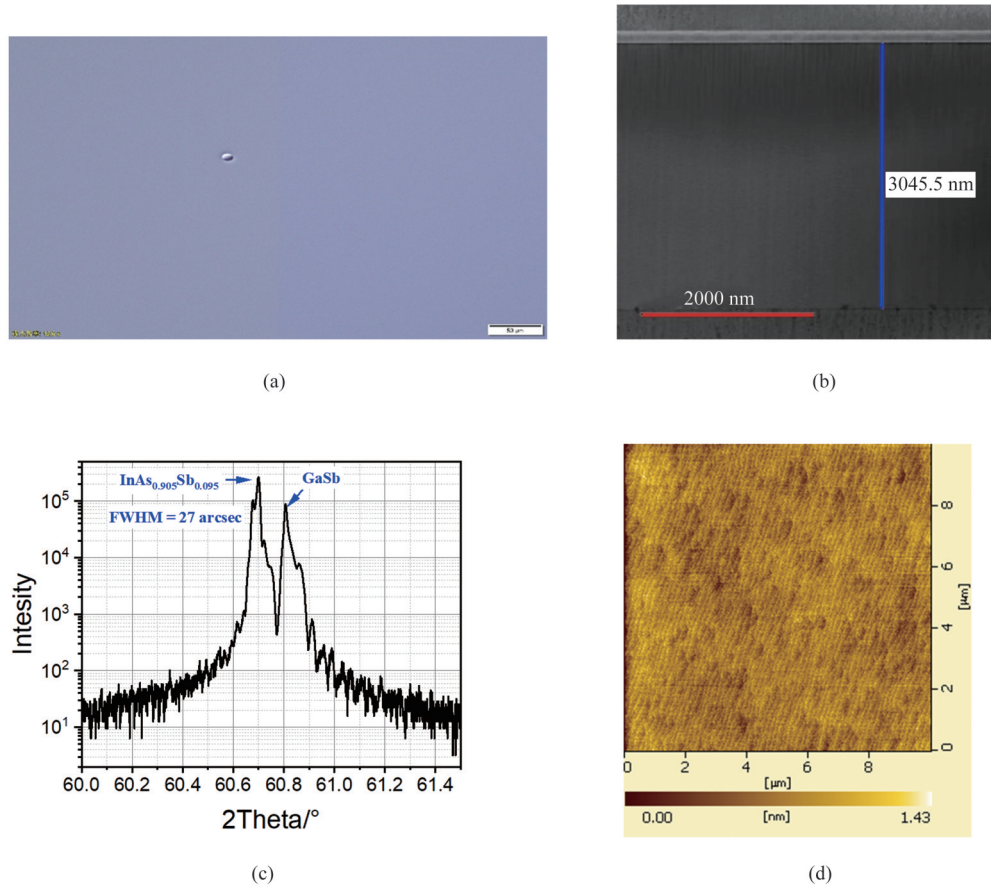
(a)

(b)

(c)

(d)

Fig. 2   (a) Nomarski microscope image under 200-times magnification; (b) the HRTEM (High-Resolution Transmission Electron Microscope) cross-section result of the XBn InAsSb sample; (c) the HRXRD (High-Resolution X-ray Diffraction) result for the XBn InAsSb sample reveals that the full width at half maximum (FWHM) of InAsSb is 27 arcsecs; (d) the Atomic Force Microscope (AFM) results for the InAsSb sample indicate a root mean square (RMS) roughness of 0.19 nm

图 2   (a) 显微镜图像，放大 200 倍；(b) XBn InAsSb 样品的高分辨透射电子显微镜（HRTEM）横截面结果；(c) XBn InAsSb 样品的高分辨 X 射线衍射（HRXRD）结果显示 InAsSb 的半峰宽（FWHM）为 27 arsecs；(d) InAsSb 样品的原子力显微镜（AFM）结果显示均方根（RMS）粗糙度为 0.19 nm
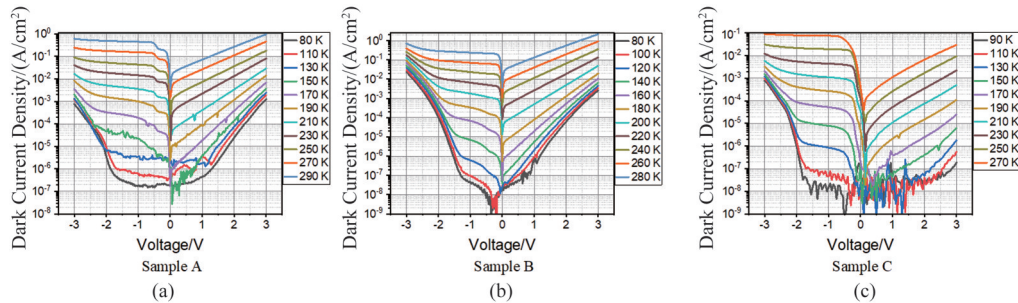

(a)

(b)

(c)

Fig. 3   (a)-(c) The dark current (J_{dark}) behavior under various temperatures and applied biases for samples A, B, and C, notably, at a temperature of 150 K and a bias voltage of -0.5 V, the dark current is measured approximately 1×10^{-5} A/cm² for both sample A and B, whereas it decreases to 5×10^{-6} A/cm² for sample C

图 3   (a)-(c)样品 A、B 和 C 在不同温度和偏置下的暗电流（J_{dark}）特性，在 150 K 温度和-0.5 V 偏压下，样品 A 和 B 的暗电流均约为 1×10^{-5} A/cm²，而样品 C 的暗电流降至 5×10^{-6} A/cm²

distinct space charge regions at the interface of the PBn structure：a）between the BL and the AL；b）between the BL and the CL.

By adjusting the p-type doping concentrations in both the BL and the CL, the tuning current and the occurrence of a 'hole trap' at the valence band can be modified. The dark current characteristics can be effectively modeled using the back-to-back diode equations[18]：

$$J_1 = J_{A1}\left(e^{-\beta V_1 V_{on1}} - 1\right) + \frac{V_1}{R_{SCP1}} \qquad , \quad (3)$$

$$J_2 = -J_{A2}\left(e^{-\beta V_2 V_{on2}} - 1\right) - \frac{V_2}{R_{SCP2}} \qquad . \quad (4)$$

The equation $\beta = q/nkT$ incorporates fundamental factors, where q is the electron charge, k stands for the

(a) Sample A

(a) Sample B
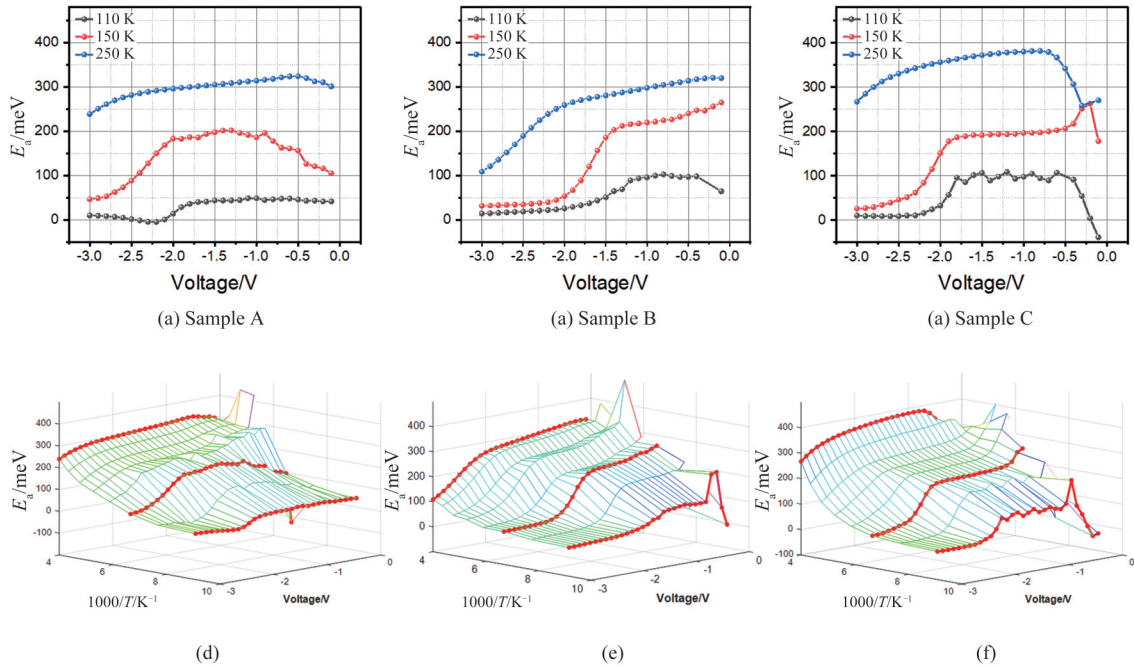
(a) Sample C

(d)

(e)

(f)

Fig. 4　(a)-(f) The E_a variations under different temperatures and applied biases for samples A, B, and C, notably, at 250 K (depicted by the solid blue circle), E_a is measured approximately 300 meV, indicating the dominance of diffusion current in the dark current. Comparatively, E_a for samples A and B is smaller than that of Sample C, signifying the onset of the SRH process affecting device performance in the BL-doped samples, at a lower temperature of 150 K, the activation energy is approximately 200 meV, accompanied by an increased proportion of G-R current within the dark current

图 4　(a)-(f)样品 A、B 和 C 在不同温度和偏置下的 E_a 变化,值得注意的是,在 250 K(如实心蓝圆所示)下,E_a 约为 300 meV,表明扩散电流在暗电流中占主导地位,相比之下,样品 A 和 B 的 E_a 小于样品 C,表明 SRH 过程对势垒层掺杂的样品的器件性能产生影响,150 K 温度下,激活能约为 200 meV,暗电流中 G-R 电流的比例增加

Boltzmann constant, T is the temperature, and n denotes the ideality factor. In our model, V_{on1} and V_{on2} represent the operating voltages under negative and positive bias, respectively. This model encompasses resistance from two space charge regions (R_{SCR1} and R_{SCR2}) and an ideality factor ($\beta = q/nkT$), which can be adjusted to account for diffusion or G-R (Generation-Recombination) currents.

We define the positive polarity as a configuration where a negative bias is applied to the n-side of diode 1 and a positive bias is applied to the p-side of diode 2. When a negative bias of $V = V_1$ is applied, it results in a current density $J = J_1$, with J_{A1} representing the plateau current and V_{on1} being the open turn-on voltage. Conversely, when a positive bias of $V = V_2$ is applied, it leads to a current density $J = J_2$, with J_{A2} representing the plateau current and V_{on2} signifying the open turn-on voltage.

This model is adept at elucidating the presence of two space charge regions at the interface of PBn structure, notably between the BL and the AL, and between the CL and the BL.

For the photocurrent of Sample C, the simulation parameters include: $n=20$, $R_{SCR1} = 1×10^9$ $\Omega \cdot cm$, $R_{SCR2} = 8×10^{10}$ $\Omega \cdot cm$, $J_{A1}=4×10^{-8}$ A/cm^2, $J_{A2} = 1×10^{-11}$ A/cm^2, $V_{on1}=-0.5$ V, $V_{on2}=-0.05$ V, and $T=77$ K.

Figure 5(b) displays the fitting of the photocurrent for Sample C, where the simulation results (indicated by the purple dashed line) closely align with the experimen-

tal results (depicted by the blue solid line). These simulation results further substantiate the existence of two space charge regions located on both sides of the barrier layer.

In Fig. 5(a), the Arrhenius fitting results of the dark current for sample C are presented under various reverse biases. At an applied bias of -0.2 V, diffusion current overwhelmingly dominates, which is approximately four times higher than the Rule 07 reference (indicated by the purple dashed line). However, under -0.5 V and -1.0 V biases, the contribution of the G-R current increases. This surge in G-R current under higher applied bias voltages may be attributed to the expansion of space charge regions.

Figure 5(b) shows the photocurrent characteristics of the three samples at 77 K. The intriguing 'second-plateau' turn-on voltage is observed in the BL p-type doped samples A and B. Notably, this turn-on voltage is exceptionally high in sample A, where the p-type doping concentration of the CL exceeds that of the BL. However, sample B shares the same 'second-plateau' turn-on voltage as sample C. This suggests that the higher p-type doping in the CL compared to the BL introduces an additional barrier in the valence band, effectively blocking the photocurrent.

The photocurrent of the sample with the UID barrier layer is aptly simulated by the back-to-back diode model, signifying the presence of two space charge regions lo-
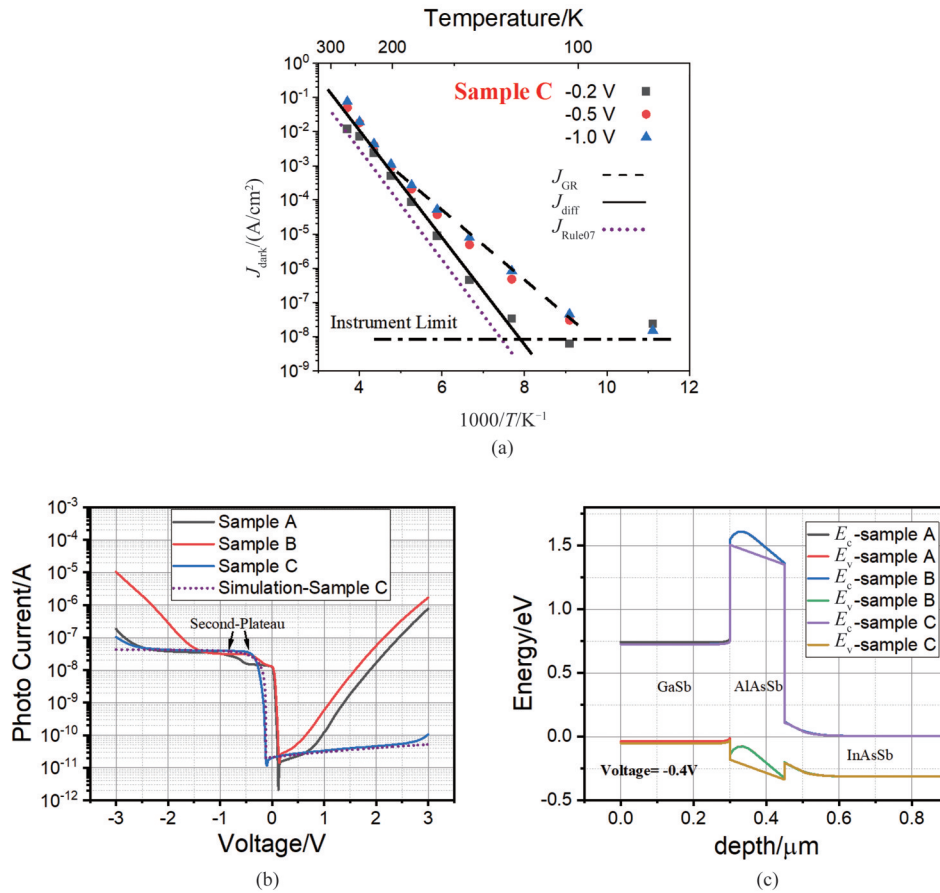
Fig. 5   (a) The Arrhenius fitting results for sample C, demonstrating the prevalence of diffusion current under low reverse bias voltage (-0.2 V), the Rule 07 reference for dark current is represented by the purple dashed line; (b) the photocurrent characteristics of the three samples are illustrated under various applied biases at 77 K, notably, the 'second-plateau' turn-on voltage is evident in samples A and B, the photocurrent *IV* for Sample C (represented by the blue solid line) is effectively fitted by the back-to-back diode model (as indicated by the purple dashed line); (c) the energy band profiles for the three samples at -0.4 V, as calculated by Silvaco

图 5   (a)样品 C 的 Arrhenius 拟合结果，表明在低反向偏压(-0.2 V)下，扩散电流占主导地位，紫色虚线表示了暗电流的 Rule 07 参考线；(b)三个样品在 77 K 下在不同施加偏置下的光电流特性，值得注意的是，样品 A 和 B 中明显出现了"第二台阶"开启电压，样品 C 的光电流 *IV*(由蓝色实线表示)采用了背靠背二极管模型进行了拟合(如紫色虚线所示)；(c)由 Silvaco 计算得到的三个样品在-0.4 V 下的能带结构

cated on both sides of the barrier layer.

When comparing the photocurrent behaviors of samples A, B, and C, it becomes evident that the p-type doping in the barrier layer introduces the distinctive 'second plateau' turn-on voltage. Silvaco simulations of the energy band structure (as shown in Fig. 5(c)) further confirm that p-type doping creates a hole trap within the valence band. At low reverse bias voltages, this hole trap restricts both the photocurrent and dark current. As the reverse bias voltage increases, the confined carriers within the hole trap can be effectively extracted.

In samples with an undoped barrier layer, the valence band remains relatively flat, and no 'second-plateau' turn-on voltage is observed. In contrast, samples with p-type doping in the barrier layer exhibit very low turn-on voltages, some even reaching positive biases. Both experimental results and theoretical calculations strongly suggest that p-type doping in the barrier layer introduces an additional barrier within the valence band.

This phenomenon can be attributed to two key factors：1）P-type doping in the BL tilts the valence band, reducing the valence band offset between the AL and the BL to zero or even to a positive bias；2）In the PBn structure, the role of the AlAsSb barrier layer in governing the dark current and photocurrent of the photodetectors predominantly depends on the interface band alignment between the BL and the AL and the high impedance of the wide bandgap AlAsSb layer.

The introduction of p-type doping at the interface between the BL and the AL effectively eliminates the barrier effect of this interface on carriers. P-type doping in the BL facilitates easy tunneling under positive bias voltage, reducing the junction impedance. This diminished barrier effect on the conduction band electrons weakens its influence on most carriers. Consequently, it allows for the transverse tunneling of electrons from the AL to the electrode layer at a lower positive bias voltage.

Conversely, samples that remain unintentionally doped in the BL do not exhibit tunneling characteristics even at a positive bias voltage of 3 V. Under these conditions, the majority of electron carriers in the AL are effectively blocked.

3　Conclusion

This study presents a comprehensive examination of PBn InAsSb photodetectors with a p-type doped BL, incorporating both simulation and experimental results. It is noteworthy that the p-type doping concentration demonstrates minimal influence on the dark current (J_{dark}). However, it significantly impacts several other key parameters, including activation energy (E_a), turn-on voltage, and tuning current.

The introduction of p-type doping creates a hole trap in the valence band of AlAsSb, leading to the emergence of the 'second plateau' turn-on voltage. This hole trap subsequently blocks both photocurrent and dark current under low reverse bias voltages. As the reverse bias voltage increases, the previously blocked carriers within the hole trap become extractable. The p-type doped BL is instrumental in facilitating tunneling at lower bias voltages.

Notably, the 'second-plateau' reverse turn-on voltage and the positive tunneling characteristics vanish in the case of the UID BL sample. In such samples, the presence of two space charge regions on either side of the UID BL plays a pivotal role in blocking the majority carriers in both the absorption and contact layers.

Through the analysis of p-type doping in InAsSb photodetectors, we gain valuable insights into transport properties and the energy band structure within PBn designs. This knowledge is instrumental for optimizing structure designs and enhancing the performance of high operating temperature (HOT) photodetectors.

The MWIR InAsSb application market is promising for a wide range of applications, because the HOT photodetectors can achieve SWaP³ (size smaller, wight lighter, performance higher, power lower and price cheaper). IRnova, SCD, Raytheon Vision Systems and Leonardo UK are developing MWIR InAsSb products for the next generation infrared equipment.

References

[1] Deng G, Yang W, Zhao P, et al. High operating temperature In-AsSb−based mid−infrared focal plane array with a band−aligned compound barrier[J]. Applied Physics Letters, 2020, 116(3): 031104.

[2] Deng G, Song X, Fan M, et al. Upside−down InAs/InAs$_{1-x}$Sb$_x$ type−II superlattice−based nBn mid−infrared photodetectors with an Al-GaAsSb quaternary alloy barrier[J]. Optics Express, 2020, 28(9): 13616−13624.

[3] Ting D Z, Fisher A M, Pepper B J, et al. Progress in InAs/InAsSb superlattice barrier infrared detectors[C]//Infrared Technology and Applications XLVIII. SPIE, 2022, 12107: 167−175.

[4] Soibel A, Ting D Z, Rafol S B, et al. Mid−wavelength infrared In-AsSb nBn detectors and FPAs with very low dark current density [J]. Applied Physics Letters, 2019, 114(16): 161103.

[5] Klipstein P C. Perspective on III－V barrier detectors[J]. Applied Physics Letters, 2022, 120(6): 060502.

[6] Klipstein P, Klin O, Grossman S, et al. MWIR InAsSb XBn detectors for high operating temperatures[C]//Infrared Technology and Applications XXXVI. SPIE, 2010, 7660: 939−947.

[7] Rogalski A, Martyniuk P, Kopytko M, et al. InAsSb−based infrared photodetectors: Thirty years later on[J]. Sensors, 2020, 20(24): 7047.

[8] Shockley W, Read Jr W T. Statistics of the recombinations of holes and electrons[J]. Physical Review, 1952, 87(5): 835.

[9] Hall R N. Electron−hole recombination in germanium[J]. Physical Review, 1952, 87(2): 387.

[10] Ting D Z Y, Soibel A, Höglund L, et al. Theoretical aspects of minority carrier extraction in unipolar barrier infrared detectors[J]. Journal of Electronic Materials, 2015, 44(9): 3036−3043.

[11] Reine M, Pinkie B, Schuster J, et al. New model for the ideal nBn infrared detector[C]//Infrared Technology and Applications XL. SPIE, 2014, 9070: 309−325.

[12] Glasmann A, Prigozhin I, Bellotti E. Understanding the CV Characteristics of InAsSb−Based nBn Infrared Detectors With N−and P−Type Barrier Layers Through Numerical Modeling[J]. IEEE Journal of the Electron Devices Society, 2019, 7: 534−543.

[13] Schuster J, Keasler C A, Reine M, et al. Numerical simulation of InAs nBn back−illuminated detectors[J]. Journal of electronic materials, 2012, 41(10): 2981−2991.

[14] Klipstein P C. XBnn and XBpp infrared detectors[J]. Journal of Crystal Growth, 2015, 425: 351−356.

[15] Du X. Mid−infrared InAs−based photodetectors: effects of processing and structures on dark currents[M]. University of Rochester, 2018.

[16] Vul A Y., Yu. A. Goldberg. Handbook Series on Semiconductor Parameters[M]. Vol. 1. edited by M. Levinshtein, S. Rumyantsev, M. Shur, 1996.

[17] Laidler K J. The development of the Arrhenius equation[J]. Journal of Chemical Education, 1984, 61(6): 494.

[18] D'Souza A I, Robinson E, Ionescu A C, InAsSb detector and FPA data and analysis[C]//Image Sensing Technologies: Materials, Devices, Systems, and Applications. SPIE, 2014, 9100: 32−40.